

RESEARCH ARTICLE | SEPTEMBER 05 2023

A scalable electronic analog of the Burridge–Knopoff model of earthquake faults

Alessio Perinelli   ; Roberto Iuppa  ; Leonardo Ricci 



Chaos 33, 093103 (2023)

<https://doi.org/10.1063/5.0161339>



View
Online



Export
Citation

CrossMark



Chaos

Special Topic: Nonautonomous Dynamics
in the Climate Sciences

Submit Today



A scalable electronic analog of the Burridge–Knopoff model of earthquake faults

Cite as: Chaos 33, 093103 (2023); doi: [10.1063/5.0161339](https://doi.org/10.1063/5.0161339)

Submitted: 9 June 2023 · Accepted: 15 August 2023 ·

Published Online: 5 September 2023 · Corrected: 6 September 2023



View Online



Export Citation



CrossMark

Alessio Perinelli,^{1,2,a)} Roberto Iuppa,^{1,2} and Leonardo Ricci^{1,3}

AFFILIATIONS

¹Department of Physics, University of Trento, 38123 Trento, Italy

²INFN-TIFPA, University of Trento, 38123 Trento, Italy

³CIMeC, Center for Mind/Brain Sciences, University of Trento, 38068 Rovereto, Italy

^{a)}Author to whom correspondence should be addressed: alessio.perinelli@unitn.it

ABSTRACT

The Burridge–Knopoff model implements an earthquake fault as a mechanical block-spring chain. While numerical studies of the model are abundant, experimental investigations are limited to a two-blocks, analog electronic implementation that was proposed by drawing an analogy between mechanical and electrical quantities. Although elegant, this approach is not versatile, mostly because of its heavy reliance on inductors. Here, we propose an alternative, inductorless implementation of the same system. The experimental characterization of the proposed circuit shows very good agreement with theoretical predictions. Besides periodic oscillations, the circuit exhibits a chaotic regime: the corresponding markers of chaoticity, namely, the correlation dimension and the maximum Lyapunov exponent, were experimentally assessed to be consistent with those provided by numerical simulations. The improved versatility and scalability of the circuit is expected to allow for experimental implementations of the Burridge–Knopoff model with a large number of blocks. In addition, the circuit can be used as the basic element of scalable platforms to investigate the dynamics of networks of oscillators and related phenomena.

© 2023 Author(s). All article content, except where otherwise noted, is licensed under a Creative Commons Attribution (CC BY) license (<http://creativecommons.org/licenses/by/4.0/>). <https://doi.org/10.1063/5.0161339>

Electronic circuits are ideal platforms to experimentally investigate the dynamics of physical systems that would otherwise be unwieldy to implement. When dealing with nonlinear systems, which can exhibit diverse dynamical regimes, an experimental verification of numerical predictions—for example, by means of electronic analogs—is crucial. In the present work, an electronic implementation of the mechanical Burridge–Knopoff model is introduced and experimentally characterized. While stemming from the modelization of geophysical phenomena, the circuit versatility makes it suitable to experimentally investigate general synchronization phenomena and chaos in complex networks of coupled nonlinear oscillators.

I. INTRODUCTION

The Burridge–Knopoff (BK) model is a mechanical model of the dynamics of faults.^{1–4} Also known as “spring-block model,” it consists of a chain of massive blocks lying on a rough, horizontal surface, each connected to the nearest neighbors by springs and linked, again by a spring, to an upper, horizontal ceiling that moves with a constant velocity with respect to the surface. The purpose

of the BK model is the description of the dynamical behavior of real faults, whereby a constant, slow driving motion of plates produces an accumulation of “stress” up to a threshold at which such stress is released through an abrupt motion—i.e., an earthquake—of one or more of the system’s constituent parts. A key feature of the system is the nonlinear dependence of the surface friction force on a block’s velocity. Different functional forms for such friction have been proposed, from a simple velocity-weakening^{5,6} to a more complex dependence on the previous state of the blocks.^{6,7} These functional forms, however, lead to similar behaviors.⁸

By relying on the numerical simulation of a one-dimensional system made of several hundred blocks, the sequence of slow accumulation and sudden release was first shown to yield a self-organized critical regime,⁹ as in the prototypical sandpile model.¹⁰ Consequently, the system undergoes events—earthquakes—whose size is distributed according to a power-law, thus reproducing the well-known Gutenberg–Richter relation¹¹ between magnitude and occurrence frequency of earthquakes. Later numerical studies of systems containing up to $\sim 10^5$ blocks, both in one¹² and two dimensions,¹³ showed that the BK model is capable of reproducing other peculiar characteristics of earthquakes. It is worth noting

that the Gutenberg–Richter power-law relation was reproduced also by considering a two-dimensional, simplified BK model in which the dynamics described by Newton's law is replaced by a cellular automaton evolution rule.^{14,15}

While there are several experimental studies on properties, like friction, that are of interest in possible mechanical realization of the BK model,^{16,17} the first known experimental implementation of the model is the two-blocks electronic analog developed in 1995 by Field, Venturi, and Nori¹⁸ (FVN). The circuit simulates the massive blocks by means of capacitive loads, and the elastic couplings by means of inductors; two complementary JFET transistors provide the nonlinear friction analog.¹⁹ An interesting property of this implementation is that, for a certain range of parameters, its dynamics exhibits a chaotic regime, which was confirmed by numerical simulations.^{20,21}

A point worth emphasizing is that, in order to study complex systems, experimental implementations provide a complementary tool to numerical approaches. While numerical experiments, also due to the availability of powerful computing machines, provide a fundamental technique to investigate complex dynamics, complex systems present features that are difficult to simulate numerically: above all, noise of unspecified color and the intrinsic variability of the elements that make up the system of interest. On the other hand, an experimental implementation, besides being naturally affected by noise, necessarily relies on nonidentical replicas of single elementary units, thus automatically emulating—though in a partially uncontrolled way—the intrinsic variability within the real system. Finally, numerical integrations of differential equations that describe a system of interest are always carried out by considering discrete time steps, thus introducing an artificially limited bandwidth, which is not the case for analog simulators.

It should be noted that departure from ideality was theoretically studied by investigating, for example, the effect of time delay in the friction response²² and by means of mean field approaches applied to BK models with added noise.^{23–25} These studies further highlighted the need of addressing the unnatural lack of variability of the basic BK model,²¹ which might lead to misleading numerical results, and at the same time call for a comparison between individual and collective behavior of blocks.²³ In this regard, further experimental implementations are required.

On the other hand, the main issue of experimental implementations is scalability. The possibly most convenient approach is provided by electronic circuits, which are used to successfully emulate and investigate systems as diverse as neurons^{26,27} and lasers.^{28–30} Nevertheless, scalability is not assured but, rather, has to be pursued by carefully selecting the elements and the devices contained in the system's blocks, as well as their mutual interaction. So, while the elegant FVN electronic analog is a good starting point toward more complex BK networks, the use of inductors to emulate the elastic couplings and the reliance on currents, rather than voltages, as analogs of mechanical positions, render this solution hardly scalable.

In this paper, we propose an improved electronic analog of the BK model that can be easily scaled to an arbitrary number of blocks. The main reason for the improved scalability is the absence of physical, typically bulky, inductors, which are replaced by suitable networks based on operational amplifiers. Instead of an inductor and two JFETs as in the FVN implementation, a single block contains

four operational amplifiers that can be promptly integrated within a single device. Moreover, while the coupling within the FVN circuit was also realized via an inductor, the implementation described here relies on an inverting operational amplifier and a coupling resistor.

The paper is organized as follows. Upon a detailed description of the dimensionless BK model and a summary of the FVN circuit in Sec. II, we discuss the improved design in Sec. III. The experimental implementation, as well as the characterization of its function, are the topics of Sec. IV: by using a bifurcation diagram, we compare the performance of the circuit with numerical simulations. The chaotic regime is quantitatively highlighted by assessing the maximum Lyapunov exponent, which is in very good agreement with numerical calculations. Future developments are discussed in Sec. V.

II. BURRIDGE-KNOPOFF MODEL AND FIELD, VENTURI AND NORI IMPLEMENTATION

A. Mechanical model

The mechanical BK model for the motion of two coupled blocks under the effect of different forces is schematically shown in Fig. 1. The upper ceiling moves with respect to the surface with a constant velocity u_d . Traditionally, the equations of motion are described in terms of the displacements x_1, x_2 of the block positions relative to the positions corresponding to relaxed k springs (and thus in the ceiling's frame), and of the velocities u_1, u_2 of the blocks in the surface frame, so that, for example $u_1 = u_d + \dot{x}_1$. One, therefore, has

$$\begin{aligned} m \frac{du_1}{dt} &= -kx_1 - k_c(x_1 - x_2) - F(u_1), \\ \frac{dx_1}{dt} &= u_1 - u_d, \\ m \frac{du_2}{dt} &= -kx_2 - k_c(x_2 - x_1) - F(u_2), \\ \frac{dx_2}{dt} &= u_2 - u_d, \end{aligned}$$

where m is the mass of each block, k is the elastic constant of the spring linking each block with the upper ceiling, k_c is the elastic constant of the spring coupling the two blocks, and $F(u)$ is the nonlinear,

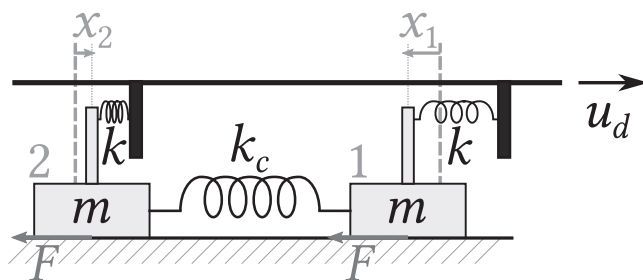


FIG. 1. Two-blocks mechanical BK model. The upper ceiling, which the blocks are coupled to via springs with elastic constant k , is dragged with constant velocity u_d with respect to the underlying surface. This surface exerts a nonlinear, velocity-dependent friction F to each block's motion.

velocity-dependent friction that the surface exerts on each block. The velocities are assumed to be non-negative.

There exists a relative freedom in the choice of the functional form of $F(u)$ vs u . The possibly simplest choice³ is a positive velocity-weakening force $F(u)$, which has to be monotonically decreasing from its maximum value at $u = 0$. A possible choice for $F(u)$ is a hyperbola⁵ given by $F(u) = F_0(1 - \sigma)^2/(1 - \sigma + u)$, where σ is a non-negative number smaller than one.

The BK model describes the interface between two plates moving in the opposite direction. The elastic continuum of real plates is approximated by the discretized blocks linked with each other.³ At the interface, real plates store elastic energy due to compressive and shear stresses:³¹ in the BK model this elastic accumulation of energy is provided by the springs. The mechanism for “loading” the system, i.e., for providing a constant, slow external driving that produces the accumulation of stress, is given by the upper ceiling moving at a constant velocity. The surface friction is the crucial ingredient that allows to simulate the stick-slip behavior of real plates: as a section of a real plate, a block is “stuck” until the force acting on it overcomes the threshold for sticking friction. The block then slides, corresponding to an earthquake-like slipping event of the plate.

B. Dimensionless system

The system describing the mechanical BK model can be rendered dimensionless by defining a dimensionless time $\tau \equiv t\sqrt{k/m}$, a dimensionless speed $v_i = u_i/u_0$ (in the following, i takes the values 1 and 2), a dimensionless position $\xi_i \equiv x_i\sqrt{k/m}/u_0$, a dimensionless friction $\varphi(v_i) \equiv \frac{F(v_i)}{u_0\sqrt{mk}}$ and, finally, the ratio $\lambda \equiv k_c/k$ of the two spring constants. The resulting system of equations reads

$$\frac{dv_i}{d\tau} = -(1 + \lambda)\xi_i + \lambda\xi_{3-i} - \varphi(v_i), \quad (1a)$$

$$\frac{d\xi_i}{d\tau} = v_i - v_d, \quad (1b)$$

with $i = 1, 2$, so that the equations are indeed four. The nonlinear function $\varphi(v_i)$ is assumed (i) to be defined only for non-negative values of v , (ii) to be positive, and (iii) to decrease down to zero from a maximum value $\varphi(0)$ that occurs at $v = 0$.

The system of equations above assumes the velocities v_i , v_d to be referred to the surface at rest. For reasons that will become clear later, one can consider a new description in which the surface moves with a positive dimensionless speed Δv , so that $v'_i = v_i + \Delta v$, $v'_d = v_d + \Delta v$. The system of equations becomes

$$\frac{dv'_i}{d\tau} = -(1 + \lambda)\xi_i + \lambda\xi_{3-i} - \varphi(v'_i - \Delta v), \quad (2a)$$

$$\frac{d\xi_i}{d\tau} = v'_i - v'_d, \quad (2b)$$

where the index i takes the values $i \in \{1, 2\}$.

C. Inductor-based FVN implementation

The general form provided by Eq. (1) was experimentally implemented by Field, Venturi, and Nori¹⁸ by drawing a direct parallelism between mechanical and electrical quantities. The idea was to consider capacitance as the electrical analog of mass, inductance as the reciprocal of an elastic constant, and voltage as the electrical analog of velocity. By replacing v_i with V_i/V_0 , where V_0 is a suitable constant voltage, v_d with V_d/V_0 , and τ with t/\sqrt{LC} , Eq. (1) becomes

$$\frac{dV_i}{dt} = \frac{V_0}{\sqrt{LC}} \left[-(1 + \lambda)\xi_i + \lambda\xi_{3-i} - \varphi\left(\frac{V_i}{V_0}\right) \right],$$

$$V_0\sqrt{LC}\frac{d\xi_i}{dt} = V_i - V_d.$$

Now, by assuming that $V_0\xi_i/\sqrt{LC}$ represents a current I_i , these last equations become

$$C\frac{dV_i}{dt} + \frac{V_0}{\sqrt{LC}}\varphi\left(\frac{V_i}{V_0}\right) + I_i = \lambda(I_{3-i} - I_i),$$

$$L\frac{dI_i}{dt} = V_i - V_d,$$

where the terms proportional to φ are currents $I_F(V_i)$ that nonlinearly depend on the respective voltages V_i 's. In all these equations, the parameter λ represents the coupling: if $\lambda = 0$, namely, in the case of no coupling, the system could be promptly implemented by using the circuit in Fig. 2 devoid of the central inductor, i.e., by assuming L_c to be infinitely large. On the other hand, letting L_c be finite leads to the current I_{12} satisfying the following equation:

$$L_c \frac{dI_{12}}{dt} = V_1 - V_2 = (V_1 - V_d) - (V_2 - V_d) = L \left(\frac{dI_1}{dt} - \frac{dI_2}{dt} \right),$$

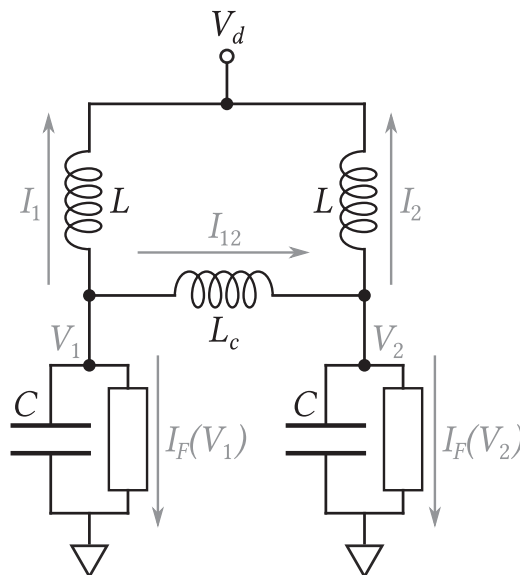


FIG. 2. Inductor-based electronic analog of the BK model of Fig. 1, as originally proposed by Field, Venturi, and Nori.¹⁸

whose integral provides $I_{12} = (I_1 - I_2)L/L_c$. Consequently, if λ is set equal to L/L_c , the circuit of Fig. 2 exactly implements the BK model. Each nonlinear element, characterized by the I-V characteristics $I_F(V_i)$, was implemented by means of a JFET-diode network with negative differential resistance,¹⁹ whose role is to hamper negative currents and provide a “triangular-like” profile in the first quadrant of the related I-V characteristic. The structure and function of this network are discussed in the original FVN work.¹⁸

Although the inductor-based implementation draws an elegant analogy between mechanical and electrical quantities, it is affected, from a practical point of view, by several drawbacks. A major issue is the presence of inductors itself. These elements are typically bulky and have intrinsically large tolerances compared with other components, leading to a relatively high uncertainty on the L, L_c values and thus on τ, λ . Moreover, the objective difficulty in tuning inductance values compromises the tunability of these parameters. Another point of concern is the fact that currents, which in the inductor-based implementation correspond to state variables, are less straightforward to measure than voltages.

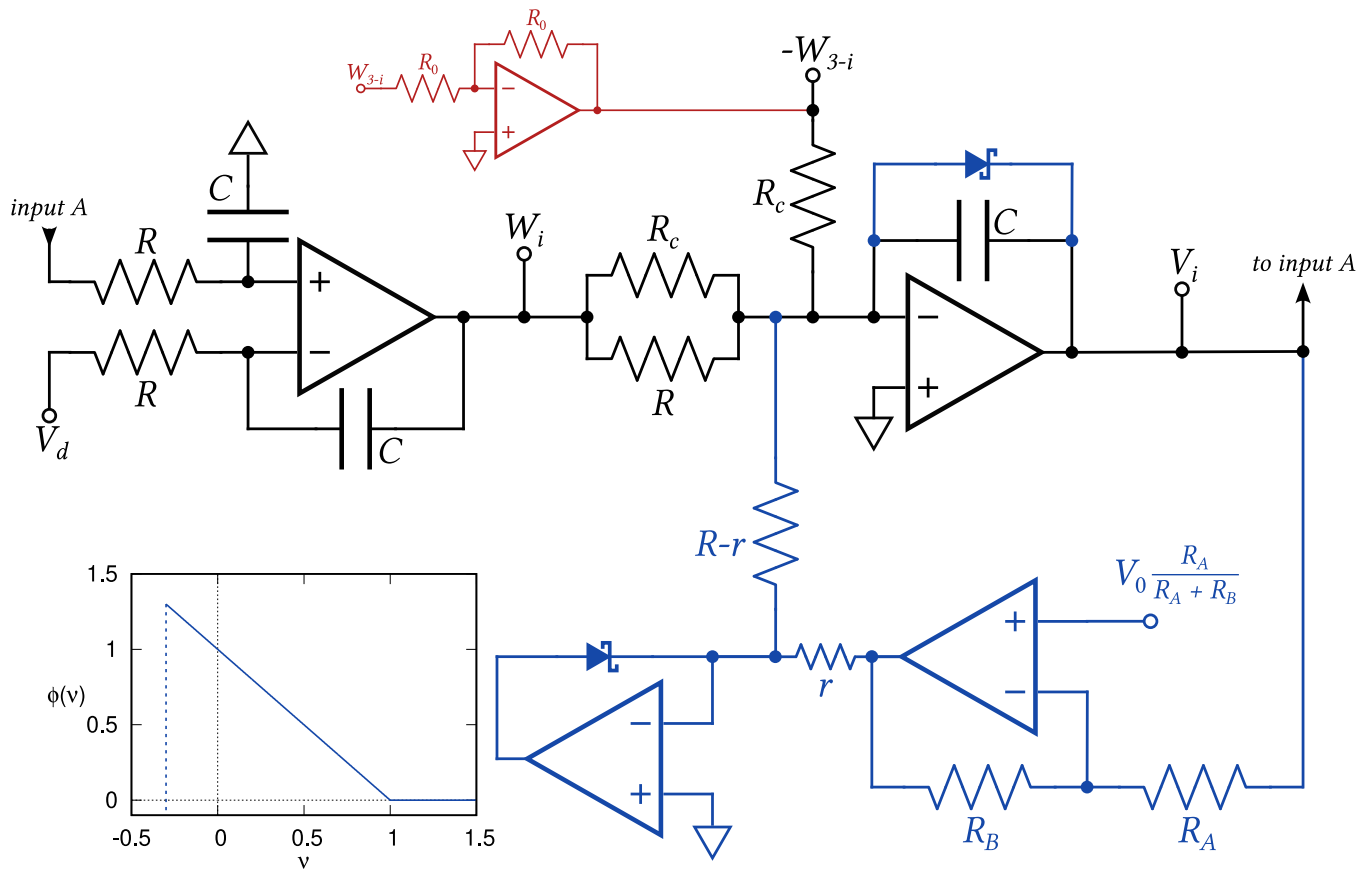


FIG. 3. Inductorless implementation of the BK model. The circuit diagram refers to a single block, labeled by i ($i = 1, 2$). The input $-W_{3-i}$ is connected to the output W_{3-i} of the other block, multiplied times -1 by means of a standard inverting operational amplifier (red). The blue part of the network refers to the nonlinear element, whose characteristic is drawn in the bottom left plot.

III. IMPROVED ELECTRONIC ANALOG

In light of the considerations expressed at the end of the previous section, an implementation based on operational amplifiers has many advantages. First, both the inductors and the nonlinear elements based on JFETs are replaced by networks containing op-amps, resistors, capacitors, and diodes. Second, the parameters that characterize the dynamics, like the circuit's characteristic time, are set via resistance values, which are more reliable than inductances in terms of nominal value and can be easily trimmed, for example, by means of digital potentiometers. Finally, the state variables v_i, ξ_i are implemented as voltages $V_i = v_i V_0, W_i = \xi_i V_0$: although the elegant analogy between electrical and mechanical quantities of the FVN implementation is lost, the system's state space can be now easily and fully sampled.

The first step consists in rewriting the differential equations as integral ones, to make use of integrators that are more stable than their differential counterparts. Setting the time constant to be given by $\tau = RC$, where R and C are suitably chosen resistance and capacitance, integrating the system of Eq. (2) for a “moving

surface,” and replacing $V'_i = V_i + \Delta V$ and $V_d = V_d + \Delta V$, where $V_d = V_0 v_d$, $\Delta V = V_0 \Delta v$, leads to the following system of equations:

$$V_i + \Delta V = -\frac{1}{RC} \int \left[(1 + \lambda) W_i - \lambda W_{3-i} + V_0 \varphi \left(\frac{V_i}{V_0} \right) \right] dt, \quad (3a)$$

$$W_i = -\frac{1}{RC} \int (V_d - V_i) dt. \quad (3b)$$

If we skip for a while the nonlinear term $V_0 \varphi \left(\frac{V_i}{V_0} \right)$ and set $\Delta V = 0$, the two integrations above can be promptly implemented by considering the black part of the circuit diagram shown in Fig. 3, where $\lambda = R/R_c$.

The next step concerns the implementation of the nonlinear term. To comply with the constraints set in Sec. II A, a Schottky diode is inserted on the feedback network of the integrator producing V_i ; the diode prevents the output voltage V_i to drop

below $-V_{\text{diode}}$, where $V_{\text{diode}} \approx 0.3$ V. This solution appears to be in contradiction with the constraint that velocity must be always non-negative. However, the constraint is fulfilled in the “moving surface reference frame” in which $\Delta V = V_{\text{diode}}$.

With regard to the nonlinear friction element, a linear drop for the analog of the velocity-weakening force is implemented as follows. The output of the rightmost of the two additional op-amps drawn in blue in Fig. 3 is given by $V_0 - V_i R_B / R_A$. Downstream of the resistor r , the voltage is prevented to drop below 0 by an active clamp made of the second op-amp drawn in blue in Fig. 3 and having a diode in its feedback network. The resulting voltage is fed back into the integrator generating V_i through an additional resistor $R - r$.

The improved implementation, which consists of two identical blocks as the one shown in Fig. 3, was built by using OP-07 op-amps and 1N5817 Schottky diodes. The op-amps were supplied with $V_{\text{CC}} = \pm 12$ V. The circuit components were selected with the following nominal values: $C = 100 \text{ nF}$, $R = R_c = 10 \text{ k}\Omega$, $R_A = R_B = 10 \text{ k}\Omega$, $r = 1.8 \text{ k}\Omega$, and $V_0 = 1$ V. This last choice is

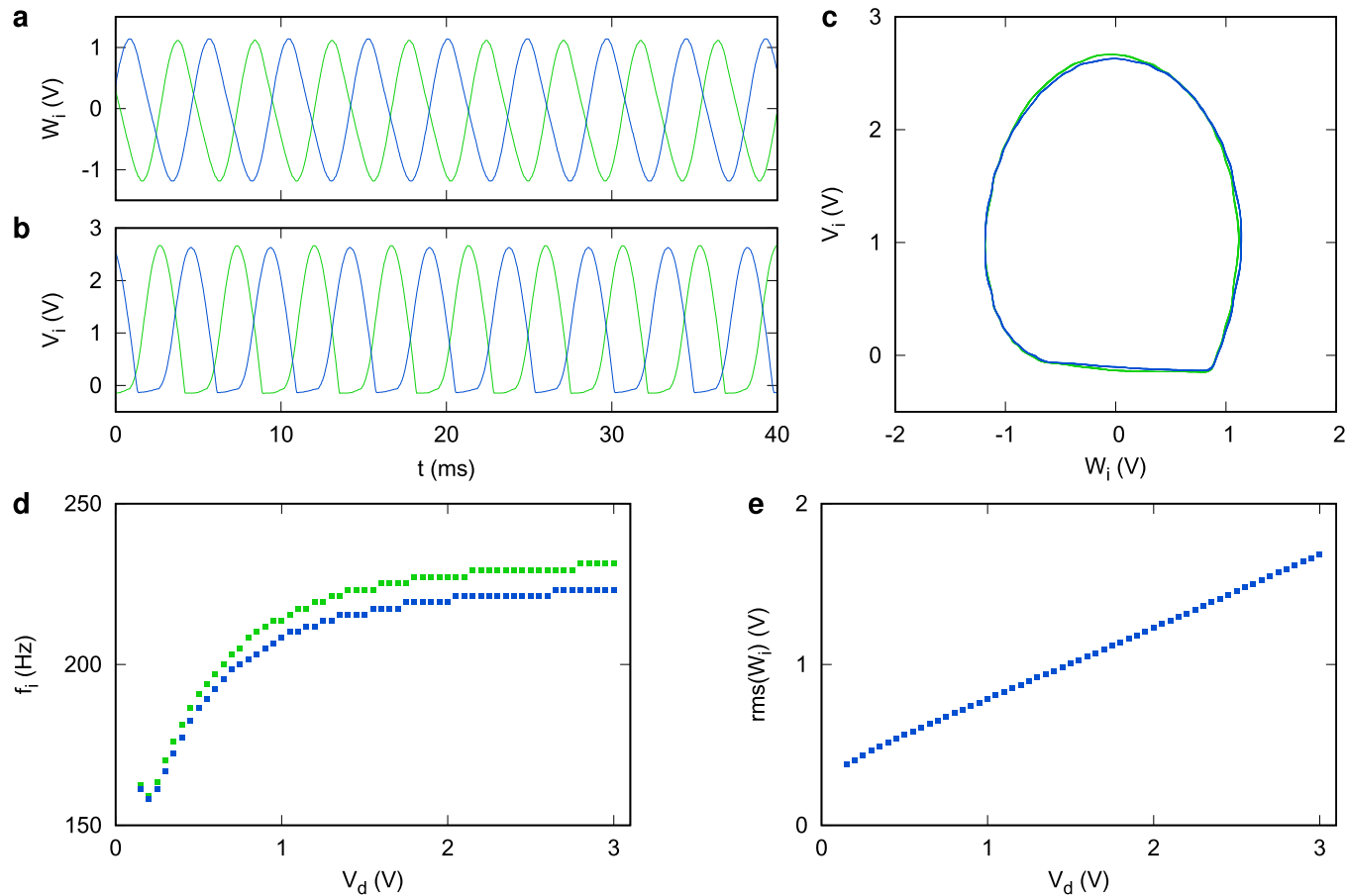


FIG. 4. Uncoupled oscillators; data for block 1 (2) are reported in blue (green). (a) Plot of W_1 , W_2 , and (b) plot of V_1 , V_2 , vs time. (c) Phase portraits (Lissajou figures) of V_1 vs W_1 and V_2 vs W_2 . The plots shown in (a)–(c) were obtained by setting $V_d = 1$ V. (d) Dependence of the oscillation frequency of the two blocks as a function of the external parameter V_d . (e) Root mean square of W_1 and W_2 as a function of the external parameter V_d .

justified by trading-off an optimal signal-to-noise ratio and the necessity to prevent the oscillating activity from approaching the saturation voltage of the operational amplifiers.

The constant voltage of 0.5 V at the noninverting input of the rightmost of the two op-amps generating the nonlinear element was provided by using a voltage divider between V_{CC} and ground. The voltage V_d was provided by means of an external source. As explained in the next section, the evolution of the four voltages V_1 , W_1 , V_2 , W_2 occurs within a bandwidth of several kilohertz. We therefore acquired them with a sampling frequency of 25 kHz.

IV. CHARACTERIZATION OF THE IMPROVED IMPLEMENTATION

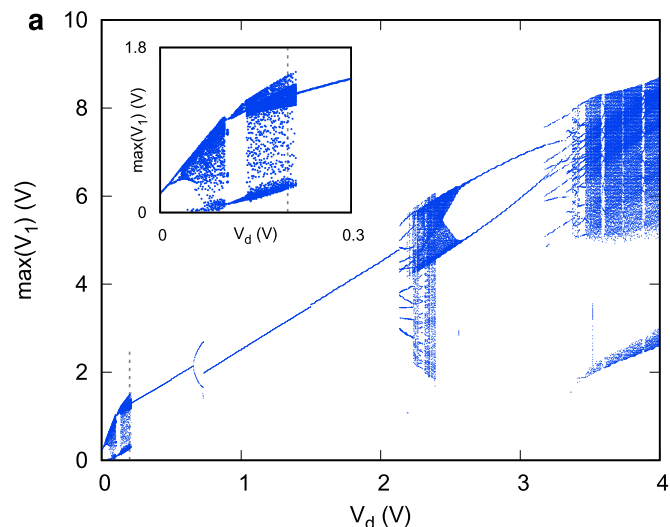
A. Single block behavior

The first characterization concerns the function of each of the two single blocks, in the absence of couplings. In this case, $\lambda = 0$ and the differential form of Eq. (3) can be promptly shown to correspond to the following second-order differential equation (the subscript i is omitted):

$$\frac{d^2V}{dt^2} + \frac{1}{\tau} \varphi' \left(\frac{V}{V_0} \right) \frac{dV}{dt} + \frac{1}{\tau^2} (V - V_d) = 0.$$

The equation is of the kind met in the classical description of stick-slip vibrations,³² i.e., of the self-sustained oscillations induced by friction.

The measured oscillating behavior is shown in Fig. 4. Both frequency and amplitude depend on the parameter V_d .



B. Two blocks bifurcation diagrams

In the presence of coupling, dynamics becomes richer. To characterize it, we considered the distribution of the local maxima of V_1 as a function of the parameter V_d , as shown in Fig. 5(a) (V_2 behaves similarly). The scan of the V_d parameter was carried out by switching off the circuit's power supply, changing the voltage V_d , and then switching the power supply back on. In this way, for each value of V_d , the recorded evolution is independent of the previous state. Values of V_d were limited to 4 V in order to prevent the operational amplifiers from reaching saturation. It is apparent that the structure of the distribution corresponds to a bifurcation diagram: while, for example, in the range $1 \text{ V} \leq V_d \leq 2 \text{ V}$ the oscillation shows only one maximum, slight changes of V_d induce a dramatic change of the dynamics, like, for example, at $V_d \simeq 0.21 \text{ V}$.

The experimentally observed behavior is confirmed by numerical integrations of Eq. (3), whose results are shown in Fig. 5(b). Numerical integration was carried out by means of a Runge–Kutta Prince–Dormand (8,9) algorithm by setting the integration time step to $10 \mu\text{s}$. An initial transient of 1 s was discarded, while maxima in the successive 3 s were recorded. Analogously to the experimental case, the initial conditions are reset at each integration: the voltages W_1 , W_2 , V_2 are set to zero, while V_1 is initialized with a random number uniformly distributed between 0 and 1. The diodes were modeled by using a Shockley equation whose parameters were determined by fitting it to an experimental I–V characteristic. Especially at values of V_d below 1 V, the experimental and numerical bifurcation diagrams are essentially the same, thus upholding the quality of the analytical description of the system.

It is worth noting that the differences between the experimental and numerical bifurcation diagrams observed at $V_d \geq 2 \text{ V}$ can be attributed, for example, to the limited bandwidth of the operational

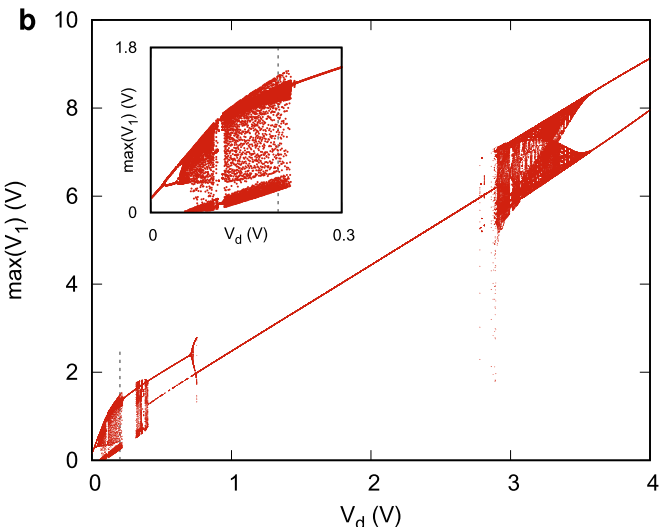


FIG. 5. Bifurcation diagrams corresponding to the experimentally implemented (a) and the numerically simulated (b) two-blocks electronic analog. In each diagram, the local maxima of V_1 are plotted as a function of the external parameter V_d , which is varied in steps of 1 mV. The insets magnify the interval $0 \leq V_d \leq 0.3 \text{ V}$. The gray dashed lines highlight the value $V_d = 0.2 \text{ V}$, which was set for the analysis of the chaotic behavior.

amplifiers and the presence of noise. Other sources of discrepancy between the experimental data and the numerical simulations can be ascribed to the nonidealities that affect the experimental system. This issue is further investigated in Sec. IV D.

At $V_d \lesssim 0.05$ V, the system undergoes period-doubling bifurcations, the first two of which can be resolved also in the experimental data. The occurrence of bifurcations is a hint of a chaotic dynamics, which is also apparent in the phase portraits of Fig. 6. These figure shows, again, experimental and numerical results obtained for $V_d = 0.2$ V, as well as the time dependence of both the position analog voltage W_1 and the velocity analog voltage V_1 . In a way this is reminiscent of a seismic behavior: the experimental and numerical plots reveal an irregular and spiky activity concerning velocity, whereas the corresponding displacements undergo slow “load” phases followed by abrupt “release” phases.

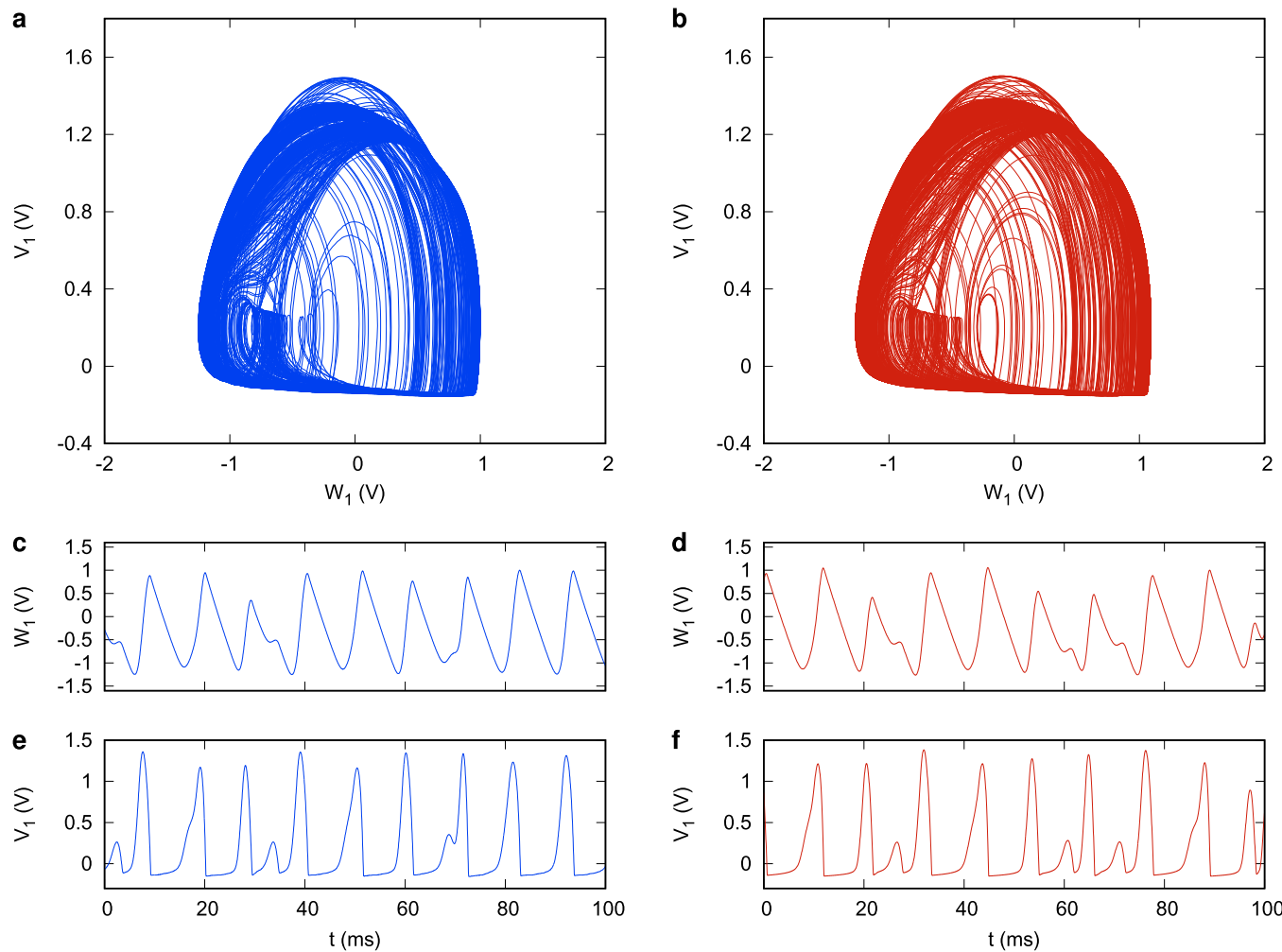


FIG. 6. Chaotic behavior of the system for $V_d = 0.2$ V. (a) Experimental and (b) numerical phase portraits of V_1 vs W_1 . Experimental time series plots of W_1 (c) and V_1 (e). Numerical time series plots of W_1 (d) and V_1 (f).

set of embedding pairs $\{m, L \mid m \in [2, m_{\max}], L \in [1, L_{\max}]\}$. Following established guidelines,³³ given a proper choice of the sampling period T , setting $m_{\max} = L_{\max} = 20$ allows to efficiently explore the uniformity region of $\hat{\nu}$. Here $T = 600 \mu\text{s}$.

Figure 7(a) shows the results of the map analysis. The presence of a uniformity region of $\hat{\nu}$ bounded by two hyperbolae is an evidence of chaos.^{33,35} This presence is also highlighted by the plot of $\hat{\nu}$ vs the embedding window $w = (m - 1)LT$, and by the histogram of $\hat{\nu}$, respectively shown in Figs. 7(b) and 7(c), respectively. Averaging $\hat{\nu}$ within the uniformity region yields 1.971 ± 0.007 .

An even more decisive evidence of a chaotic behavior emerges from the assessment of the maximum Lyapunov exponent (MLE),

evaluated on the experimental time series by using the divergence rate method.^{37,38} The results are shown in Fig. 7(d), which plots experimental MLE values vs w . A cluster of values at about 45 Hz occurs at the lower end of the embedding window interval that is compatible with the uniformity region inferred by using the correlation dimension analysis. These values coincide—within the statistical error—with the numerical value $\text{MLE} = (46 \pm 5) \text{ Hz}$ that was determined by numerically integrating Eq. (1) and applying the so-called standard method.^{39,40} The related, numerically evaluated, Kaplan–Yorke dimension⁴¹ ν_{KY} turns out to be 2.0027 ± 0.0004 . This value is in line with the average correlation dimension expressed above. It is worth noting that, in general,⁴² $\nu_{\text{KY}} > \nu$. For

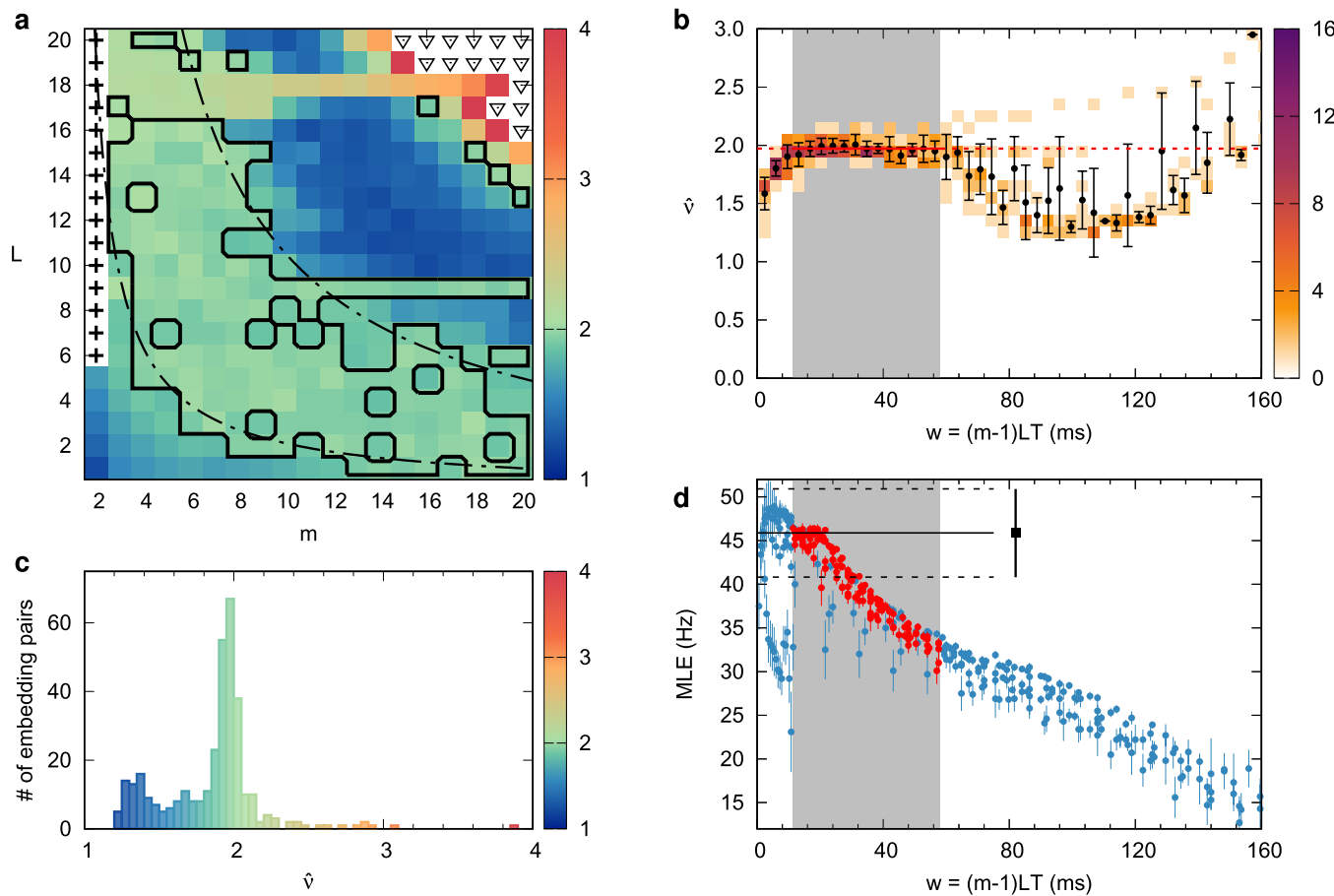


FIG. 7. “Chasing chaos” analysis of the experimental W_1 time series obtained by setting $V_d = 0.2 \text{ V}$. (a) Map of estimated correlation dimension $\hat{\nu}$ vs. embedding pair (m, L) . Pairs marked with “+” provide embedded sequences that are deemed to be incompatible with a finite-dimensional source.³³ Black triangles mark pairs for which $\hat{\nu}$ is unavailable due to excessive computational time. The black solid line encompasses the pairs contained in the three bins corresponding to the peak of the histogram in (c) ($1.90 \leq \hat{\nu} \leq 2.05$). The black, dash-dotted hyperbolae, defined by $w = 11.4 \text{ ms}$, $w = 58.2 \text{ ms}$ bound the region of uniform $\hat{\nu}$ corresponding to the interval of the embedding window w highlighted in gray in (b) and (d). (b) Sample joint distribution of $(w, \hat{\nu})$ for the $\hat{\nu}$ -map in (a). Bin width is 0.1 along the $\hat{\nu}$ axis and 3.6 ms along the w axis. Black dots and the related errorbars correspond to the expected value and the related uncertainty of $\hat{\nu}$ for each given value (bin) of w . A uniformity region, highlighted in gray, is identified at $11.4 \text{ ms} \leq w \leq 58.2 \text{ ms}$. (c) Histogram of the estimated $\hat{\nu}$; the bin width is 0.05. (d) Distribution of MLE as a function of w . Each point and the related uncertainty corresponds to the value assessed on an embedding pair by using the divergence rate method. Points marked in red correspond to pairs whose w belongs to the uniformity region of (b), also highlighted in gray here, and yielding a $\hat{\nu}$ belonging to the peak in (c). The black dot (errorbar) corresponds to the value (uncertainty) of MLE numerically assessed via the standard method.

the sake of completeness, we also report the full Lyapunov spectrum obtained by means of the standard method. The values of the exponents are: $\text{MLE} = \lambda_1 = (46 \pm 5) \text{ Hz}$, $\lambda_2 = -(0.3 \pm 0.3) \text{ Hz}$, $\lambda_3 = -(17.2 \pm 0.8) \times 10^3 \text{ Hz}$, $\lambda_4 = -(27.5 \pm 0.4) \times 10^3 \text{ Hz}$. Because the second exponent λ_2 is compatible with zero, a single positive Lyapunov exponent is present, so that the system's dynamics corresponds to low-dimensional chaos.

D. Sources of discrepancy between experimental and numerical behavior

As mentioned in Sec. IV B, the bifurcation diagrams observed for the experimental implementation of the circuit and the related numerical simulation, although qualitatively similar, exhibit some quantitative discrepancies. These discrepancies can be attributed to departures from ideality affecting the experimental system that are not modeled within the numerical simulation. Possibly the most relevant sources of these issues are the mismatch between real values and nominal ones for the discrete components, and the difference of these real values between the two blocks.

These sources of nonideality were numerically investigated by means of a “perturbative” approach, in which only one parameter is changed at a time. We first considered a lowering of the R_c resistance

by 2% ($9.8 \text{ k}\Omega$ instead of $10 \text{ k}\Omega$) for both blocks. It is worth highlighting that this discrepancy is of the same order of the tolerance on the corresponding component. As a second test, we considered a 2% asymmetry between the capacitance C of the first block, set to 98 nF , and of the second block, set to 102 nF . The bifurcation diagrams resulting from these tests are shown in Fig. 8. The experimental and numerical diagrams of Fig. 5 are also reported for the sake of comparison.

These simulations show that the presence of perturbations affects the behavior of the numerically integrated system in a way that, at least for some of the features of the bifurcation diagram, brings the corresponding diagram to a closer match to the experimentally observed one.

Most notably, both the reduction of R_c to $9.8 \text{ k}\Omega$ and the 2% asymmetry in capacitance result in a shift toward lower V_d values of the complex structure observed for $2.5 \text{ V} \lesssim V_d \lesssim 4 \text{ V}$: in both cases the structure is closer to the position at which that structure is observed in the experimental case (as highlighted by the “ \times ” symbol and the two triangles). A second feature that—at least qualitatively—can be reproduced by reducing R_c to $9.8 \text{ k}\Omega$, and thus by increasing the strength of coupling, is the multiple-period behavior that is observed in the experimental diagram for $V_d \simeq 2.2 \text{ V}$ and corresponds to about 10 well-separated lines in the diagram. Indeed, a hint of a similar behavior is observed in Fig. 8(f) for $V_d \simeq 2.4 \text{ V}$. This

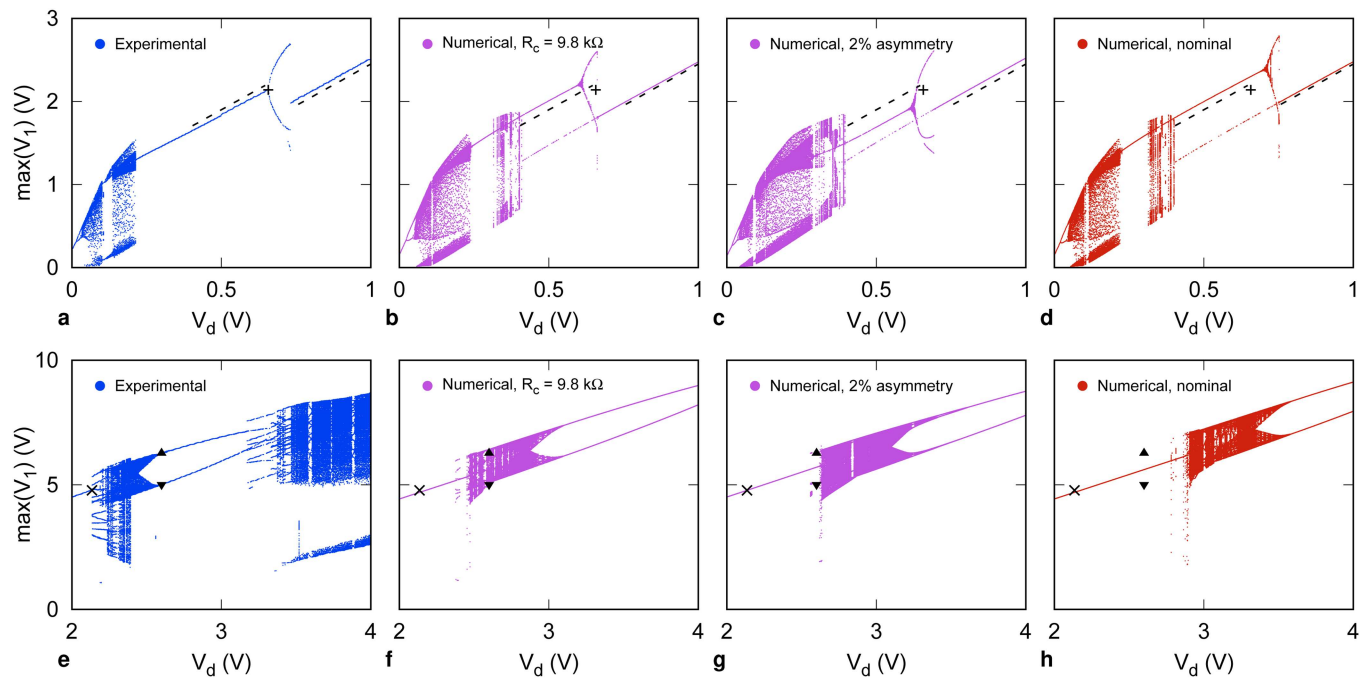


FIG. 8. Comparison between the bifurcation diagrams obtained out of the experimental implementation (a) and (e), the numerical simulation with $R_c = 9.8 \text{ k}\Omega$ (b) and (f), the numerical simulation with 2% capacitance asymmetry (c) and (g) and the numerical simulation with nominal values (d) and (h). Plots (a)–(d) display the part of the diagram close to the origin, while the plots (e)–(h) display V_d values between 2 V and 4 V. The data in (a) and (e) correspond to those in Fig. 5(a), while data in (d) and (h) correspond to those in Fig. 5(b). Black markers and dashed lines provide visual cues highlighting the remarkable points observed in the experimental bifurcation diagram: dashed lines outline the single-period limit-cycles for $0.4 \text{ V} \lesssim V_d \lesssim 1 \text{ V}$; the “+” symbol corresponds to the period-doubling bifurcation at $V_d \simeq 0.7 \text{ V}$; the “ \times ” symbol corresponds to the largest value of V_d for which the experimental system exhibits a single-period limit-cycle; the triangles denote the points at which the experimental system first exhibits a double-period limit-cycle that is visible for $2.7 \text{ V} \lesssim V_d \lesssim 3.2 \text{ V}$.

might suggest that the nonperiodic behavior of the experimental system for $V_d \gtrsim 3.1$ V could be the result of an additional, spurious coupling between the two blocks.

Finally, an effect of asymmetry is visible in the shape of the double-period behavior at $V_d \simeq 0.02$ V, corresponding to two separated lines: while the numerical integration with nominal values provides a larger separation with respect to the experimental one, the results of Fig. 8(c) match the experimental data more closely. The same consideration applies to the shape of the bifurcation at $V_d \simeq 0.7$ V: the “roundness” that characterizes the experimental data is also present in the numerical integration with asymmetry of Fig. 8(c), while it is absent in Fig. 8(d).

Despite the perturbations considered here only concern one parameter at a time, their effects, shown in Fig. 8, provide valuable hints on how the deviations of real component values from the nominal ones can affect the system’s behavior. Finally, one should also consider two other features that were not modeled in the numerical integration, namely, the nonideal behavior of operational amplifiers, most notably their finite bandwidth and slew rate, and the presence of noise. The former feature could definitely play a role for higher V_d values, where the oscillation amplitudes approach the saturation voltage of the operational amplifiers.

In summary, it is worth noting that just changing a parameter by an amount compatible with the tolerances of the electronic components might lead to significant changes in the bifurcation diagrams, without changing their basic “topology.”

V. DISCUSSION

The experimentally assessed behavior of the improved, electronic analog of the BK model discussed in the present work matches the behavior predicted by numerically integrating the differential equations that describe the system. The behavior also qualitatively coincides with the one exhibited by the former design proposed by Field, Venturi, and Nori.¹⁸

The type of devices used to implement the circuit allows for assembling a single block on a rectangular printed circuit board with sides as small as a few centimeters. The design is therefore suitable to develop networks of blocks connected both in a one-dimensional or a two-dimensional fashion, thus allowing for experimental investigations of more realistic implementations of the BK model.

Seismic noise was shown to play a role in the dynamics of the BK model.^{23–25} The versatility of the present electronic analog also allows to experimentally test these results by injecting—upon a suitable modelization, which is however beyond the scope of the present work—an external noisy signal into the system.

It is worth noting that the circuit can be also used, independently of its geophysical purpose, as a basic block to engineer complex networks of oscillators in order to investigate, for example, synchronization phenomena^{26,43} and fractal-like structures.⁴⁴ Moreover, because the driving voltage V_d can be delivered to blocks by means of simple digital-to-analog converters, it is straightforward to design experiments in which V_d is dynamically modulated, thus allowing, for example, to investigate the effect of external perturbations on earthquake fault models.⁴

ACKNOWLEDGMENTS

The authors thank the Italian Space Agency for the financial support under the contract ASI “LIMADOU Scienza+” n. 2020-31-HH.0.

AUTHOR DECLARATIONS

Conflict of Interest

The authors have no conflicts to disclose.

Author Contributions

Alessio Perinelli: Formal analysis (equal); Methodology (equal); Writing – original draft (equal). **Roberto Iuppa:** Validation (equal); Writing – review & editing (equal). **Leonardo Ricci:** Formal analysis (equal); Methodology (equal); Writing – original draft (equal).

DATA AVAILABILITY

The data that support the findings of this study are available from the corresponding author upon reasonable request.

REFERENCES

- ¹R. Burridge and L. Knopoff, “Model and theoretical seismicity,” *Bull. Seismol. Soc. Amer.* **57**, 341–371 (1967).
- ²H. Nakanishi, “Complex behavior in earthquake dynamics,” *Int. J. Mod. Phys. B* **12**, 273–284 (1998).
- ³H. Kawamura, T. Hatano, N. Kato, S. Biswas, and B. K. Chakrabarti, “Statistical physics of fracture, friction, and earthquakes,” *Rev. Mod. Phys.* **84**, 839–884 (2012).
- ⁴I. Franović, S. Kostić, M. Perc, V. Klinshov, V. Nekorkin, and J. Kurths, “Phase response curves for models of earthquake fault dynamics,” *Chaos* **26**, 063105 (2016).
- ⁵J. M. Carlson, “Two-dimensional model of a fault,” *Phys. Rev. A* **44**, 6226–6232 (1991).
- ⁶J. R. Rice and A. L. Ruina, “Stability of steady frictional slipping,” *J. Appl. Mech.* **50**, 343–349 (1983).
- ⁷B. Erickson, B. Birnir, and D. Lavallée, “A model for aperiodicity in earthquakes,” *Nonlin. Proc. Geophys.* **15**, 1–12 (2008).
- ⁸B. E. Shaw, “Frictional weakening and slip complexity in earthquake faults,” *J. Geophys. Res. Solid Earth* **100**, 18239–18251 (1995).
- ⁹J. M. Carlson and J. S. Langer, “Properties of earthquakes generated by fault dynamics,” *Phys. Rev. Lett.* **62**, 2632–2635 (1989).
- ¹⁰P. Bak and C. Tang, “Earthquakes as a self-organized critical phenomenon,” *J. Geophys. Res.-Sol. Ea.* **94**, 15635–15637 (1989).
- ¹¹B. Gutenberg and C. F. Richter, “Frequency of earthquakes in California,” *Bull. Seismol. Soc. Am.* **34**, 185–188 (1944).
- ¹²T. Mori and H. Kawamura, “Simulation study of the one-dimensional Burridge–Knopoff model of earthquakes,” *J. Geophys. Res. Solid Earth* **111**, B07302 (2006).
- ¹³T. Mori and H. Kawamura, “Simulation study of the two-dimensional Burridge–Knopoff model of earthquakes,” *J. Geophys. Res. Solid Earth* **113**, B06301, 2008). <https://doi.org/10.1029/2007JB005219>
- ¹⁴H. Nakanishi, “Cellular-automaton model of earthquakes with deterministic dynamics,” *Phys. Rev. A* **41**, 7086–7089 (1990).
- ¹⁵Z. Olami, H. J. S. Feder, and K. Christensen, “Self-organized criticality in a continuous, nonconservative cellular automaton modeling earthquakes,” *Phys. Rev. Lett.* **68**, 1244–1247 (1992).
- ¹⁶C. Mei, S. Barbot, and W. Wu, “Period-multiplying cycles at the transition between stick-slip and stable sliding and implications for the Parkfield period-doubling tremors,” *Geophys. Res. Lett.* **48**, e2020GL091807 (2021).

- ¹⁷A. Gualandi, D. Faranda, C. Marone, M. Cocco, and G. Mengaldo, “Deterministic and stochastic chaos characterize laboratory earthquakes,” *Earth Planet. Sci. Lett.* **604**, 117995 (2023).
- ¹⁸S. Field, N. Venturi, and F. Nori, “Marginal stability and chaos in coupled faults modeled by nonlinear circuits,” *Phys. Rev. Lett.* **74**, 74–77 (1995).
- ¹⁹L. O. Chua, J. Yu, and Y. Yu, “Bipolar—JFET—MOSFET negative resistance devices,” *IEEE Trans. Circuits Syst.* **32**, 46–61 (1985).
- ²⁰V. B. Ryabov and H. M. Ito, “Multistability and chaos in a spring-block model,” *Phys. Rev. E* **52**, 6101–6112 (1995).
- ²¹M. de Sousa Vieira, “Chaos and synchronized chaos in an earthquake model,” *Phys. Rev. Lett.* **82**, 201–204 (1999).
- ²²S. Kostić, N. Vasović, I. Franović, and K. Todorović, “Dynamics of simple earthquake model with time delay and variation of friction strength,” *Nonlin. Proc. Geophys.* **20**, 857–865 (2013).
- ²³N. Vasović, S. Kostić, I. Franović, and K. Todorović, “Earthquake nucleation in a stochastic fault model of globally coupled units with interaction delays,” *Commun. Nonlin. Sci. Numer. Simulat.* **38**, 117–129 (2016).
- ²⁴S. Kostić, N. Vasović, I. Franović, K. Todorović, V. Klinshov, and V. Nekorkin, “Dynamics of fault motion in a stochastic spring-slider model with varying neighboring interactions and time-delayed coupling,” *Nonlin. Dyn.* **87**, 2563–2575 (2017).
- ²⁵S. Kostić, N. Vasović, K. Todorović, and I. Franović, “EFFECT of colored noise on the generation of seismic fault MOVEMENT: Analogy with spring-block model DYNAMICS,” *Chaos Soliton. Fract.* **135**, 109726 (2020).
- ²⁶L. Minati, P. Chiesa, D. Tabarelli, L. D’Incerti, and J. Jovicich, “Synchronization, non-linear dynamics and low-frequency fluctuations: Analogy between spontaneous brain activity and networked single-transistor chaotic oscillators,” *Chaos* **25**, 033107 (2015).
- ²⁷L. Minati, M. Frasca, N. Yoshimura, L. Ricci, P. Oświecimka, Y. Koike, K. Masu, and H. Ito, “Current-starved cross-coupled CMOS inverter rings as versatile generators of chaotic and neural-like dynamics over multiple frequency decades,” *IEEE Access* **7**, 54638–54657 (2019).
- ²⁸R. Meucci, S. Euzzor, F. T. Arecchi, and J.-M. Ginoux, “Minimal universal model for chaos in laser with feedback,” *Int. J. Bifurcat. Chaos* **31**, 2130013 (2021).
- ²⁹L. Ricci, A. Perinelli, M. Castelluzzo, S. Euzzor, and R. Meucci, “Experimental evidence of chaos generated by a minimal universal oscillator model,” *Int. J. Bifurcat. Chaos* **31**, 2150205 (2021).
- ³⁰M. Castelluzzo, M. Cescato, L. Ricci, R. Meucci, and A. Perinelli, “Experimental implementation of a laser model with cavity loss modulation,” in *2022 IEEE Workshop on Complexity in Engineering (COMPENG)* (IEEE, 2022), pp. 1–5.
- ³¹J. M. Carlson, J. S. Langer, and B. E. Shaw, “Dynamics of earthquake faults,” *Rev. Mod. Phys.* **66**, 657–670 (1994).
- ³²K. Popp and P. Stelter, “Stick-slip vibrations and chaos,” *Philos. Trans. Roy. Soc. A* **332**, 89–105 (1990).
- ³³A. Perinelli and L. Ricci, “Chasing chaos by improved identification of suitable embedding dimensions and lags,” *Chaos* **30**, 123104 (2020).
- ³⁴P. Grassberger and I. Procaccia, “Characterization of strange attractors,” *Phys. Rev. Lett.* **50**, 346–349 (1983).
- ³⁵A. Perinelli and L. Ricci, “Identification of suitable embedding dimensions and lags for time series generated by chaotic, finite-dimensional systems,” *Phys. Rev. E* **98**, 052226 (2018).
- ³⁶L. Ricci, A. Perinelli, and M. Franchi, “Asymptotic behavior of the time-dependent divergence exponent,” *Phys. Rev. E* **101**, 042211 (2020).
- ³⁷J. Gao and Z. Zheng, “Local exponential divergence plot and optimal embedding of a chaotic time series,” *Phys. Lett. A* **181**, 153–158 (1993).
- ³⁸M. Franchi and L. Ricci, “Statistical properties of the maximum Lyapunov exponent calculated via the divergence rate method,” *Phys. Rev. E* **90**, 062920 (2014).
- ³⁹G. Benettin, L. Galgani, A. Giorgilli, and J. Strelcyn, “Lyapunov characteristic exponents for smooth dynamical systems and for Hamiltonian systems: A method for computing all of them. Part 1: Theory,” *Meccanica* **15**, 9 (1980).
- ⁴⁰G. Benettin, L. Galgani, A. Giorgilli, and J. Strelcyn, “Lyapunov characteristic exponents for smooth dynamical systems and for Hamiltonian systems: A method for computing all of them. Part 2: Numerical application,” *Meccanica* **15**, 21 (1980).
- ⁴¹J. L. Kaplan and J. A. Yorke, “Chaotic behavior of multidimensional difference equations,” in *Functional Differential Equations and Approximation of Fixed Points*, edited by H. Peitgen and H. Walther (Springer, Berlin, 1979), pp. 204–227.
- ⁴²P. Grassberger and I. Procaccia, “Measuring the strangeness of strange attractors,” *Physica D* **9**, 189–208 (1983).
- ⁴³L. Minati, H. Ito, A. Perinelli, L. Ricci, L. Faes, N. Yoshimura, Y. Koike, and M. Frasca, “Connectivity influences on nonlinear dynamics in weakly-synchronized networks: Insights from Rössler systems, electronic chaotic oscillators, model and biological neurons,” *IEEE Access* **7**, 174793–174821 (2019).
- ⁴⁴L. Minati, M. Frasca, G. Giustolisi, P. Oświecimka, S. Drożdż, and L. Ricci, “High-dimensional dynamics in a single-transistor oscillator containing Feynman–Sierpiński resonators: Effect of fractal depth and irregularity,” *Chaos* **28**, 093112 (2018).